Climate Dynamics (2002) 20: 31–44
DOI 10.1007/s00382-002-0257-5

S.J. Ghan · X. Bian · A.G. Hunt · A. Coleman

The thermodynamic influence of subgrid orography in a global climate model

Received: 5 September 2001 / Accepted: 29 March 2002 / Published online: 8 June 2002

Abstract Assessments of the impacts of climate change typically require information at scales of 10 km or less. Such a resolution in global climate simulations is unlikely for at least two decades. We have developed an alternative to explicit resolution that provides a framework for meeting the needs of climate change impact assessment much sooner. We have applied to a global climate model a physically based subgrid-scale treatment of the influence of orography on temperature, clouds, precipitation, and land surface hydrology. The treatment represents subgrid variations in surface elevation in terms of fractional area distributions of discrete elevation classes. For each class it calculates the height rise/descent of air parcels traveling through the grid cell, and applies the influence of the rise/descent to the temperature and humidity profiles of the elevation class. Cloud, radiative, and surface processes are calculated separately for each elevation class using the same physical parametrizations used by the model without the subgrid orography parametrization. The simulated climate fields for each elevation class can then be distributed in post-processing according to the spatial distribution of surface elevation within each grid cell. Parallel 10-year simulations with and without the subgrid treatment have been performed. The simulated temperature, precipitation and snow water are mapped to 2.5-minute (~5 km) resolution and compared with gridded analyses of station measurements. The simulation with the subgrid scheme produces a much more realistic distribution of snow water and significantly more realistic distributions of temperature and precipitation than the simulation without the subgrid scheme. Moreover, the 250-km grid cell means of most other fields are virtually unchanged by the subgrid scheme. This suggests that the tuning of the climate model without the subgrid scheme is also applicable to the model with the scheme.

S.J. Ghan (✉) · X. Bian · A.G. Hunt · A. Coleman
Pacific Northwest National Laboratory,
PO Box 999, MSIN K9-24, Richland,
Washington 99352, USA
E-mail: steve.ghan@pnl.gov

1 Introduction

Assessments of the impacts of climate change typically require information at scales of 10 km or less. In regions with complex terrain, much of the spatial variability in climate (temperature, precipitation, and snow water) occurs on scales below 10 km (Daly et al. 1994; Leung et al. 1996; Gyalistras et al. 1998).

The grid size of global climate model simulations of climate change is presently 200–300 km (Delworth and Knutson 2000; Emori et al. 1999; Flato et al. 2000; Gordon et al. 2000; Russell and Rind 1999; Washington et al. 2000; Zhang et al. 2000). Although one can expect the grid size to continue to decrease with time as computer speed and memory increase, the large increase in computer power required to reduce grid size (an eightfold increase in speed for a halving of the grid size) limits the rate of grid size reduction to a halving roughly every six years. In spite of concerted efforts, one therefore cannot expect the explicit resolution of global climate model simulations to reach that required for impact assessment for another two decades.

This gap between the resolution required for impact assessment and the resolution available from global climate models (Ghan 1992; von Storch 1995) has led to the development of a variety of downscaling techniques. These include high-resolution global atmospheric models run for selected time slices (Cubasch et al. 1995; May and Roeckner 2001), regional climate modeling (Dickinson et al. 1989; Giorgi 1990; Giorgi and Mearns 1999), and a variety of statistical downscaling methods (von Storch 1995; Wilby and Wigley 1997; Gyalistras et al. 1998; Murphy 1999, 2000). Each of these methods offers advantages but also has serious limitations.

Yet another downscaling technique is the Leung and Ghan (1995, 1998) treatment of the subgrid influence of orography on temperature, clouds, precipitation, and land surface processes. LG have shown that in a regional climate model the treatment greatly improves the simulation of snow water and significantly improves the simulation of temperature and precipitation in regions with complex terrain. To date such a treatment has not been applied to a global model.

We describe the application of the LG scheme to a developmental version of the National Center for Atmospheric Research community climate model (ccm3.10). Section 2 describes the LG scheme and its implementation in ccm3.10. Section 3 evaluates the performance of the scheme. Section 4 reviews the computational impact of the scheme. The strengths and weaknesses of the scheme are summarized in Sect. 5.

2 Subgrid Treatment

The LG scheme is based on the combination of a statistical representation of subgrid variations in surface elevation and a simple model of airflow over terrain. Subgrid variations in surface elevations are represented by a simple classification of surface elevation within each grid cell, with a fine (30 second, about 1 km) resolution surface elevation dataset used to calculate the fractional area and mean elevation of each elevation class within each grid cell. The fractional area is used for forming area-weighted grid cell means to treat the feedback of the subgrid scale to the grid scale. The mean surface elevation is used by the airflow model.

The airflow model is based on studies of airflow over topography, which suggest that airflow over mountains is limited by the potential energy barrier of the topography. The airflow model predicts a height rise/descent for each elevation class and each model layer, which can be used to diagnose the vertical profiles of temperature and humidity for each elevation class from the grid cell mean profiles.

The orographic profiles of temperature and humidity are not applied directly to the model physics to determine clouds and precipitation. Such a treatment yields an orographic signature that is much stronger than observed (LG 1995). Instead, the orographic profiles are treated as forcing terms in prognostic conservation equations for temperature and humidity applied to each elevation class,

$$\frac{\partial X_{kn}}{\partial t} = A_{kn} + D_{kn} + Q_{kn} + \frac{X^*_{kn} - X_{kn}}{\tau} \tag{1}$$

where X_{kn} is temperature or water vapor mixing ratio for class n and layer k, A is the advective tendency (including the adiabatic expansion term for temperature), D is the horizontal diffusion tendency, Q is the physics tendency, X_{kn}* is the orographic forcing value, and τ is an orographic time scale.

The treatment of each term in Eq. (1) requires special care to ensure that mass, energy, and moisture are conserved by the subgrid scheme. Conservation is essential, since the grid cell mean of the physics tendency feeds back to the conservation equation for the grid cell mean temperature and humidity.

To show conservation of energy and moisture, multiply Eq. (1) by the fractional area f_n and the layer mass m_{kn} and sum over all classes with the grid cell:

$$\sum_n f_n m_{kn} \frac{\partial X_{kn}}{\partial t} = \sum_n f_n m_{kn}(A_{kn} + D_{kn} + Q_{kn}) + \frac{1}{\tau}\sum_n f_n m_{kn}(X^*_{kn} - X_{kn}) \tag{2}$$

Conservation of mass, energy and moisture requires the following conditions:

$$\sum_n f_n = 1 \tag{3}$$

$$\sum_n f_n m_{kn} = \bar{m}_k \tag{4}$$

$$\sum_n f_n m_{kn} A_{kn} = \bar{m}_k \bar{A}_k \tag{5}$$

$$\sum_n f_n m_{kn} D_{kn} = \bar{m}_k \bar{D}_k \tag{6}$$

$$\sum_n f_n m_{kn} Q_{kn} = \bar{m}_k \bar{Q}_k \tag{7}$$

$$\sum_n f_n m_{kn} X^*_{kn} = \bar{m}_k \bar{X}_k \tag{8}$$

$$\sum_n f_n m_{kn} X_{kn} = \bar{m}_k \bar{X}_k \tag{9}$$

where the overbar denotes the grid cell mean. Condition (3) can be enforced in the processing of the high-resolution surface elevation database.

To ensure condition (4) we express m_{kn} in terms of its functional dependence on the surface pressure of class n and a normalization factor:

$$m_{kn} = m_k(p_n)\bar{m}_k / \sum_i f_i m_k(p_i) \tag{10}$$

The functional dependence of layer thickness on surface pressure depends on the definition of the vertical coordinate. For the η coordinate used in the ccm,

$$m_k(p_n) \equiv p_0 \Delta A_k + p_n \Delta B_k \tag{11}$$

where p_0 is a constant pressure and

$$p_n = \bar{p}\exp[-(z_n - \bar{z})/H] \tag{12}$$

is the surface pressure for class n, with z_n the surface elevation for class n and H the density scale height.

Conditions (5) and (6) can be guaranteed if we assume

$$A_{kn} = \bar{A}_k \tag{13}$$

$$D_{kn} = \bar{D}_k \tag{14}$$

and apply condition (4). However, to prevent the formation of negative water vapor mixing ratios the advective tendency for water vapor should be scaled to reduce the advective tendency of the highest elevation classes. An effective scaling that also maintains water conservation (i.e., satisfies Eq. 5 if Eqs. 4 and 9 are satisfied) is

$$A_{kn} = X_{kn}\bar{A}_k / \bar{X}_k \tag{15}$$

This treatment of the advective tendency replaces Eq. (13) only when the advective tendency of moisture is negative (which is when it is needed), because Eq. (15) produces an exponential instability when the advective tendency is positive. Condition (6) is satisfied if it is used to determine $\bar{Q}_k$.

Condition (8) requires the most consideration. It can be satisfied if we assume $X^*_{kn} = \bar{X}_k$. However, such a treatment does not allow any flexibility in the representation of airflow (such as limits on the height rise of air parcels). Moreover, it depends upon the definition of the vertical coordinate, producing no orographic signature for layers for which B = 0 (i.e., layers that are constant pressure). A more flexible way to ensure Eq. (8) is to diagnose the orographic profile X'_{kn} from the airflow model and then normalize it to ensure that Eq. (8) is satisfied:

$$X^*_{kn} = X'_{kn}\bar{m}_k\bar{X}_k / \sum_i f_i m_{ki} X'_{ki} \tag{16}$$

This permits any treatment of height rise.

Condition (9) will be satisfied if all of the other conditions are satisfied. That is, with the other conditions (2) becomes

$$\sum_n f_n m_{kn} \frac{\partial X_{kn}}{\partial t} = \bar{m}_k (\bar{A}_k + \bar{D}_k + \bar{Q}_k) + \frac{1}{\tau} \left(X^*_{kn} - \sum_n f_n m_{kn} X_{kn} \right) \quad (17)$$

Subtracting the grid cell mean balance

$$\bar{m}_k \frac{\partial \bar{X}_k}{\partial t} = \bar{m}_k (\bar{A}_k + \bar{D}_k + \bar{Q}_k) \quad (18)$$

from Eq. (17) yields

$$\sum_n f_n m_{kn} \frac{\partial X_{kn}}{\partial t} = \bar{m}_k \frac{\partial \bar{X}_k}{\partial t} + \frac{1}{\tau} \left(\bar{m}_k \bar{X}_k - \sum_n f_n m_{kn} X_{kn} \right) . \quad (19)$$

This means $\sum_n f_n m_{kn} X_{kn}$ relaxes toward $\bar{m}_k \bar{X}_k$, so that Eq. (9) will be satisfied.

It is important to note that Eq. (1) requires separate estimates of the physics tendencies of temperature and humidity for each elevation class. Consistent coupling of the atmosphere and land surface (e.g., more clouds at higher elevations affecting downward radiative fluxes at the surface) therefore requires that the land surface physics be treated separately for each elevation class. Thus, the subgrid scheme produces separate estimates of temperature, water vapor mixing ratio, all atmospheric physics terms, all land surface variables and all land surface physics terms for each elevation class. Although this adds a significant computational burden to the model, it also provides unprecedented detail in the final product because all of the subgrid fields can be distributed in postprocessing according to the high-resolution distribution of surface elevation. Such detail comes without the much higher cost in either speed or memory required for explicit resolution of all scales down to 10 km or less.

3 Evaluation

As a demonstration of the performance of the subgrid scheme in a global climate model, here we present and evaluate results from the last 10 years of an 11 year and 4 month simulation. The simulation is performed by ccm3.10, which is a developmental version of ccm3 (Kiehl et al. 1998) that includes the Rasch and Kristjansson (1998) prognostic cloud condensate scheme, the Collins (2001) cloud overlap treatment of radiative transfer, and the semi-lagrange dynamical core (Williamson and Olson 1994). The simulation is performed at T42 spectral resolution (2.8°, about 250 km) with 30 layers using prescribed monthly sea-surface temperatures and sea ice for the period September 1978–December 1989 and a zonally averaged ozone climatology. The elevation classification is based on a compromise balancing the need to resolve a variety of elevations within each grid cell and the need to limit the computational burden of the subgrid scheme; a maximum of twelve classes are treated in each grid cell, with elevation ranges bounded at elevations of –500, –1, 200, 400, 700, 1000, 1500, 2000, 3000, 4000, 5000, 7000, and 9000 m. Elevation classes with less than 0.01% coverage in a grid cell are assimilated into the elevation class closer to the class with the largest fractional coverage in the cell. The Global Land One-km Base Elevation (GLOBE 1999) 30-second surface elevation dataset is used to estimate the fractional area and average elevation for each elevation class and grid cell. The orographic time scale τ is prescribed at 10 hours based on our experience with the subgrid scheme in a regional climate model (LG 1998). The land surface model is initialized with 'arbitrary initialization', with the same surface type assumed for each elevation class in a grid cell. None of the physical parametrizations in ccm3.10 have been modified, except through their application to each elevation class.

The variables simulated for each elevation class are mapped according to the 2.5 minute (about 5 km) distribution of surface elevation using linear interpolation in elevation and bilinear interpolation in latitude and longitude. Although finer resolution distribution is possible, Daly et al. (1994) and LG (1998) conclude that the precipitation simulation is most accurate for a resolution of about 2.5 minutes; finer resolution may be more appropriate for temperature and snow cover, which respond to altitude more rapidly than precipitation.

Before comparing the simulation with observations, we first compare with a parallel simulation without the subgrid scheme. We hope to demonstrate that (a) the model with the subgrid scheme conserves energy and moisture as well as the model without, and (b) that for most fields the grid cell mean simulated with the subgrid scheme is indistinguishable from that simulated without. By comparing with observations we hope to show that the simulation with the subgrid scheme provides a more realistic climate at subgrid scales.

Table 1 summarizes the global mean energy and moisture balance for the simulations with and without the subgrid scheme. The global mean precipitation and evaporation agree to within less than 0.02% with the subgrid scheme, which is comparable to the atmospheric water storage during the simulation. The difference in

Table 1 Global annual means

	1 class	12 classes
Precipitation (mm/day)	2.9882	2.9800
Evaporation (mm/day)	2.9884	2.9805
Solar TOA (Wm^{-2})	234.5	235.8
Clear sky solar TOA (Wm^{-2})	283.8	283.5
IR TOA (Wm^{-2})	233.2	234.9
Clear sky IR TOA (Wm^{-2})	264.1	265.1
Solar surface (Wm^{-2})	168.6	170.1
IR surface (Wm^{-2})	62.0	63.4
Radiative heating (Wm^{-2})	–105.3	–105.8
Surface sensible and latent heating (Wm^{-2})	107.1	107.7
Cloud water path ($g\ m^{-2}$)	49.1	47.5
Water vapor path ($kg\ m^{-2}$)	22.3	22.0
Snow water equivalent (m)[a]	0.99	1.24
Volumetric soil water content ($m^3\ m^{-3}$)[a]	0.373	0.371
Total runoff (mm/day)[a]	0.622	0.759
Land to atmosphere CO_2 flux ($\mu mol\ CO_2\ m^{-2}\ s^{-1}$)[a]	–0.30	–0.12
Photosynthesis rate ($\mu mol\ CO_2\ m^{-2}\ s^{-1}$)[a]	2.40	2.20

[a] land mean only

the water balance in the simulations with and without the subgrid scheme is about 0.2%. The latter difference is small compared with present uncertainty in observations of precipitation and evaporation.

For the global heat balance at the top-of-the-atmosphere there is a systematic difference of 1–2 Wm^{-2} between the simulations with and without the subgrid scheme. The difference is smallest for the clear sky solar flux (only 0.3 Wm^{-2}), which suggests that the difference is primarily associated with clouds. Although part of the difference in the solar flux might be due to the sublinear dependence of cloud albedo on optical depth, much of it is undoubtedly due to the reduction of the column integrated cloud water from a global mean value of 49.1 g m^{-2} without the subgrid scheme to 47.5 g m^{-2} with the subgrid scheme. However, even the clear sky infrared flux differs by 1 Wm^{-2}, which suggests a role for water vapor (the global mean column integral decreases from 22.3 kg m^{-2} without to 22.0 kg m^{-2} with the subgrid scheme) as well (surface temperature decreases slightly with the subgrid scheme, so it can't explain the increase in the clear sky). The difference between the net radiation imbalance (net absorbed solar minus outgoing infrared) simulated at the top of the atmosphere with and without the subgrid scheme (0.4 Wm^{-2}) is smaller than the imbalance in either simulation (1.3 and 0.9 Wm^{-2}), suggesting that the impact of the subgrid scheme on the radiation balance is smaller than the tuning of the radiation balance and hence can be considered negligible.

Comparing the radiative heating of the atmosphere with the heating by surface fluxes of sensible and latent heat, there is an imbalance of about 2 Wm^{-2} for both simulations. One should not expect a perfect balance between radiative heating and the surface fluxes because frictional dissipation also contributes about 2 Wm^{-2} heating, but accounting for heating by frictional dissipation makes the imbalance even worse. The imbalance is due to a lack of energy conservation by this version of the semi-lagrange dynamical core of the model (D. Williamson personal communication). It is nearly the same for both simulations, and is larger than the difference between the radiative heating or surface fluxes simulated with and without the subgrid scheme (0.6 Wm^{-2}). The fact that the imbalance is nearly identical for both simulations suggests that the subgrid scheme is not introducing a spurious source or sink of energy.

Table 1 also summarizes the global and annual means of several important land surface variables. The subgrid scheme increases snow water significantly, as might be expected because of the nonlinear dependence of snowfall and snowmelt on temperature and hence elevation. As will be shown later, the 25% global increase is much smaller than local changes because the global mean is dominated by the prescribed 1 m snow water in Antarctica. Although the global soil moisture is relatively insensitive to the subgrid scheme, the global runoff increases 22%. As might be expected from the nonlinear dependence of runoff on precipitation and hence elevation, most of the increase in runoff occurs in mountainous terrain. The global mean net flux of CO_2 from the land to the atmosphere is reduced in magnitude from –0.30 to –0.12 μmol CO_2 m^{-2} s^{-1} with the subgrid scheme. Such a large reduction arises because the net flux is upward in some regions and downward in others, so that the global mean flux is sensitive to the small upward shift in the flux that is simulated in many regions with the subgrid scheme. Bonan (1998) found an even greater sensitivity in the global mean flux with slightly different versions of CCM3. The global mean photosynthetic rate, which is always positive, is reduced by 10% with the subgrid scheme.

Figure 1 shows the global distribution of the difference between the annual mean grid-cell mean surface air temperature simulated with and without the subgrid scheme. The magnitude of the difference is less than 2 °C almost everywhere and is less than 1 °C everywhere except in most of the Arctic and Antarctica, much of the Middle East, and small parts of North America and China. The magnitude of the differences is much smaller than the magnitude of the biases in the surface air temperature simulated by CCM3 (Bonan 1998) and is less than twice the standard deviation of the annual means for all but a few grid cells. This indicates an insignificant impact of the subgrid scheme on the grid cell mean surface air temperature.

Figure 2 shows the spatial distribution of the ratio of the annual mean grid-cell mean precipitation rate simulated with to that without the subgrid scheme. The subgrid scheme changes the mean precipitation by a factor more than 1.1 over roughly half of the land and just a small fraction of ocean. For a small fraction of land points the subgrid scheme changes precipitation by a factor of 1.5 or more (i.e., the ratio is less than 0.7 or more than 1.5). Precipitation increases tend to occur along coastal mountain ranges; decreases are mostly in continental interiors presumably as a consequence of the enhanced trapping of moisture by the coastal mountains.

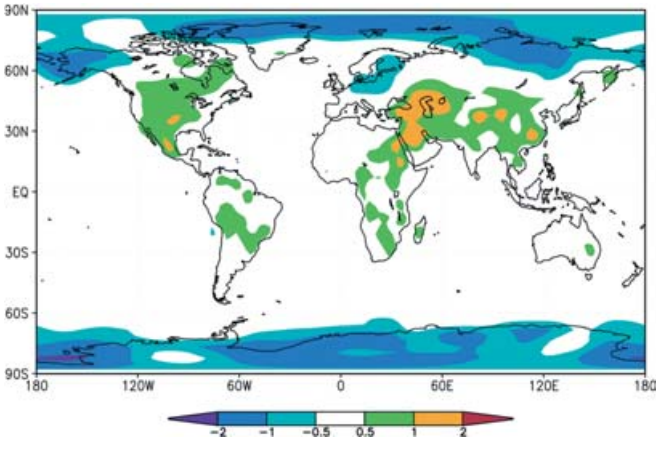

Fig. 1 Difference between annual and grid cell mean surface air temperature (°C) simulated with and without the subgrid scheme

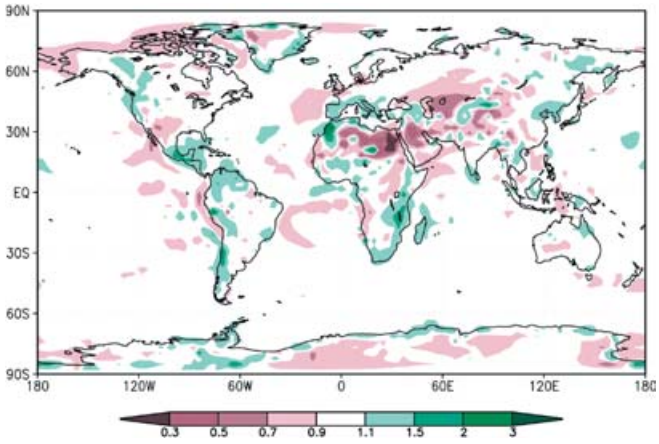

Fig. 2 Ratio of annual and grid cell mean precipitation rate simulated with and without the subgrid scheme

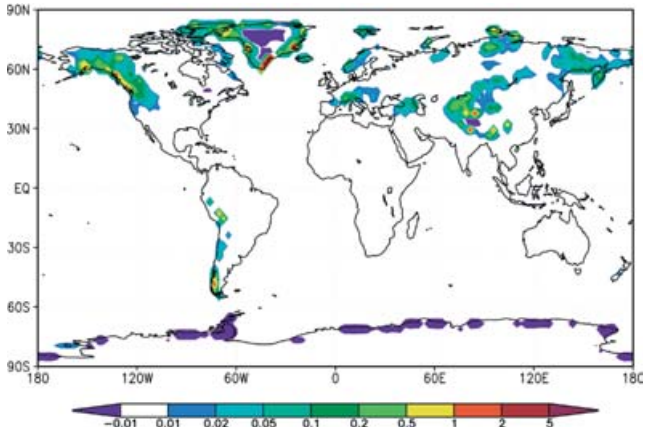

Fig. 4 Difference between annual and grid cell mean snow water equivalent (m) simulated with and without the subgrid scheme

To put these changes in perspective, Fig. 3 shows the spatial distribution of the ratio of the annual precipitation simulated without the subgrid scheme to the observed estimate of Xie and Arkin (1996). Biases exceeding a factor of 1.5 are much more common than in Fig. 2, not only over ocean (which is to be expected) but also over land. This suggests that the impact of the subgrid scheme on grid cell mean precipitation is typically much smaller than the biases. In some regions (southern Europe, Morocco, Egypt, Arabia, central Asia) the subgrid scheme appears to reduce precipitation biases, but in others (Central America, Antarctica) it increases them.

Figure 4 shows the spatial distribution of the difference between the grid-cell mean annual mean snow water simulated with and without the subgrid scheme. The subgrid scheme decreases snow water slightly along portions of the coastline of Antarctica and the interior of Greenland, but increases it substantially in the west coast ranges of North America, the Andes, the coast of Greenland, the Alps, the Caucasus, the Himalayan range, the Tibetan Plateau, and the eastern Siberia. Such increases are to be expected given the nonlinear dependence of snow water on both temperature and humidity. The decrease in the interior of Greenland is understandable, given the increase along the coast.

We now compare the subgrid simulation with observations. Observed climatologies at 2.5 minute resolution are rare for regions larger than a few hundred km. One such dataset is the PRISM precipitation and surface air temperature climatology for the continental USA compiled by Daly et al. (1994, 1997). It combines station measurements with empirical relationships between temperature/precipitation and surface elevation to produce a gridded distribution of temperature and precipitation at a spatial resolution of 2.5 minutes (about 5 km). The simulated temperature and precipitation climatology has been mapped to the same resolution, which LG 1998 found to be optimal for precipitation. Our evaluation of the simulation will be restricted to the western USA where the orographic signature is strongest and hence most sensitive to the application of the subgrid scheme.

Figure 5 compares the ''observed'' distribution of annual mean surface air temperature in the western USA with that simulated with and without the subgrid scheme. The simulation without the subgrid scheme reproduces the largest scale features of temperature, but cannot resolve the small-scale structure evident in the PRISM analysis. The simulation with the subgrid scheme captures much of the observed small-scale structure, including the low temperatures along both minor and major mountain ranges and the higher temperatures in the adjacent valleys. However, a systematic cold bias is apparent. To quantify the bias and to compare it with the simulation without the subgrid scheme, Fig. 6 shows the spatial distributions of the difference between simulated and observed annual mean temperature for both simulations. The cold bias is evident in both simulations, but the simulation without the subgrid scheme exhibits a larger cold bias in the mountain valleys and a larger warm bias on the highest

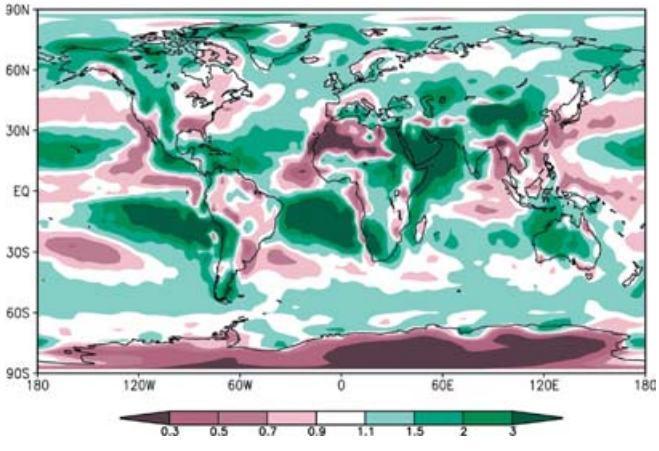

Fig. 3 Ratio of simulated/observed annual mean precipitation rate for the simulation without the subgrid scheme

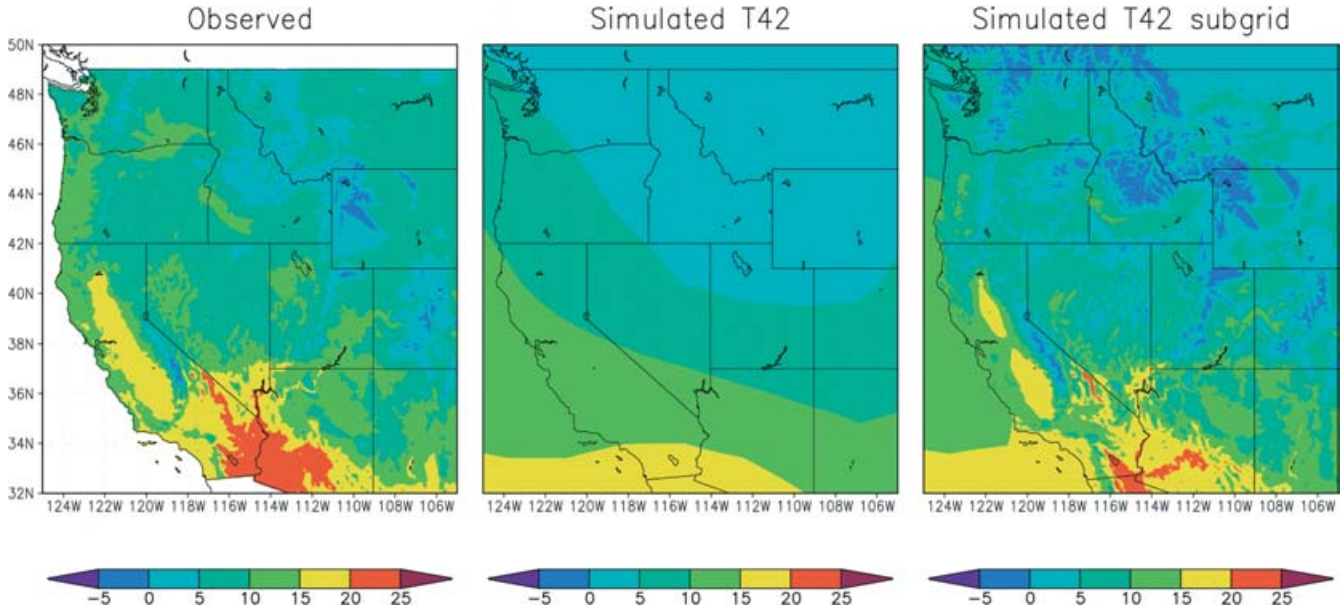

Fig. 5 Annual mean surface air temperature (°C) observed (*left*), simulated at T42 resolution without the subgrid scheme (*middle*) and simulated with the subgrid scheme (*right*), mapped to 2.5 minute resolution for the western USA

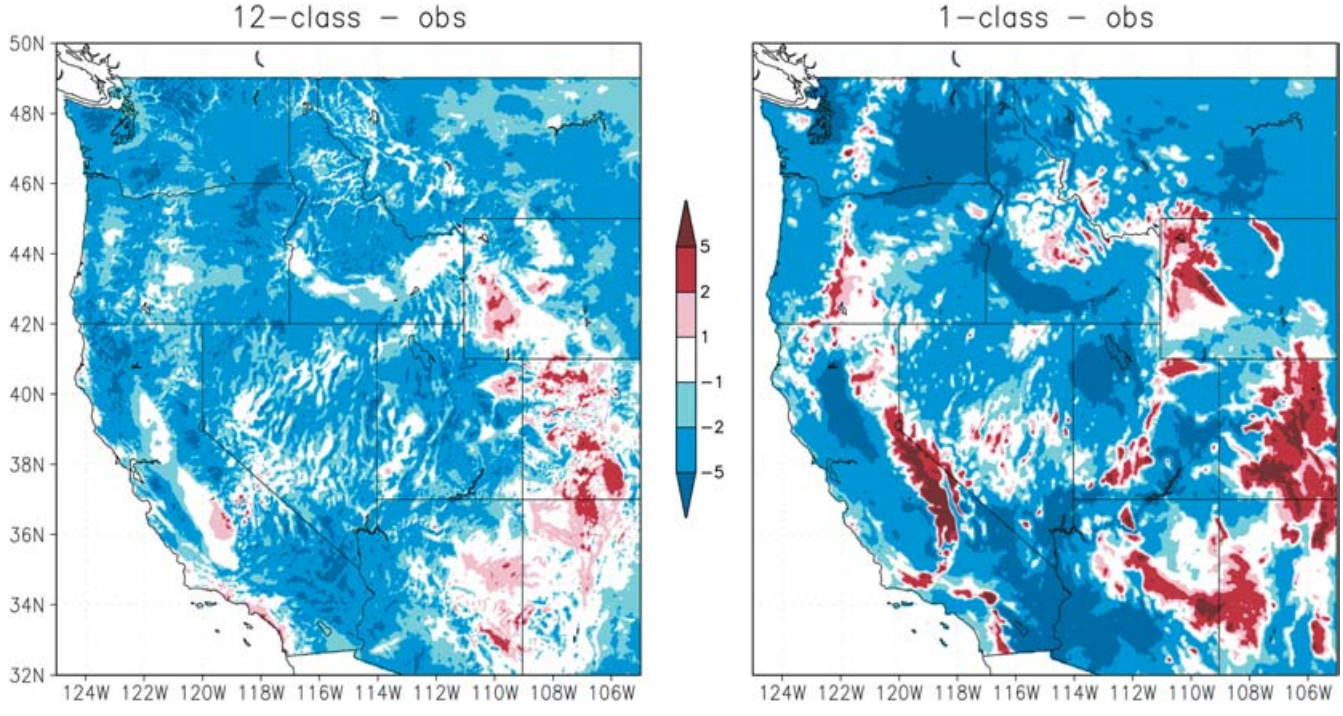

Fig. 6 Difference between simulated and observed annual mean surface air temperature (°C) for the simulations with (*left*) and without (*right*) the subgrid scheme

mountains, almost completely missing the orographic signature on temperature. The simulation with the subgrid scheme overestimates the signature somewhat, with an excessive lapse rate between the central valley of California and the Sierra Nevada range, and between the Snake River valley in southern Idaho and the surrounding mountains.

Figure 7 compares the ''observed'' annual mean precipitation rate for the western USA with that simulated with and without the subgrid scheme. The simulation without the subgrid scheme produces only the continental scale features of precipitation: dry in the southwest USA and moist in the Pacific Northwest and in the central USA. The simulation with the subgrid

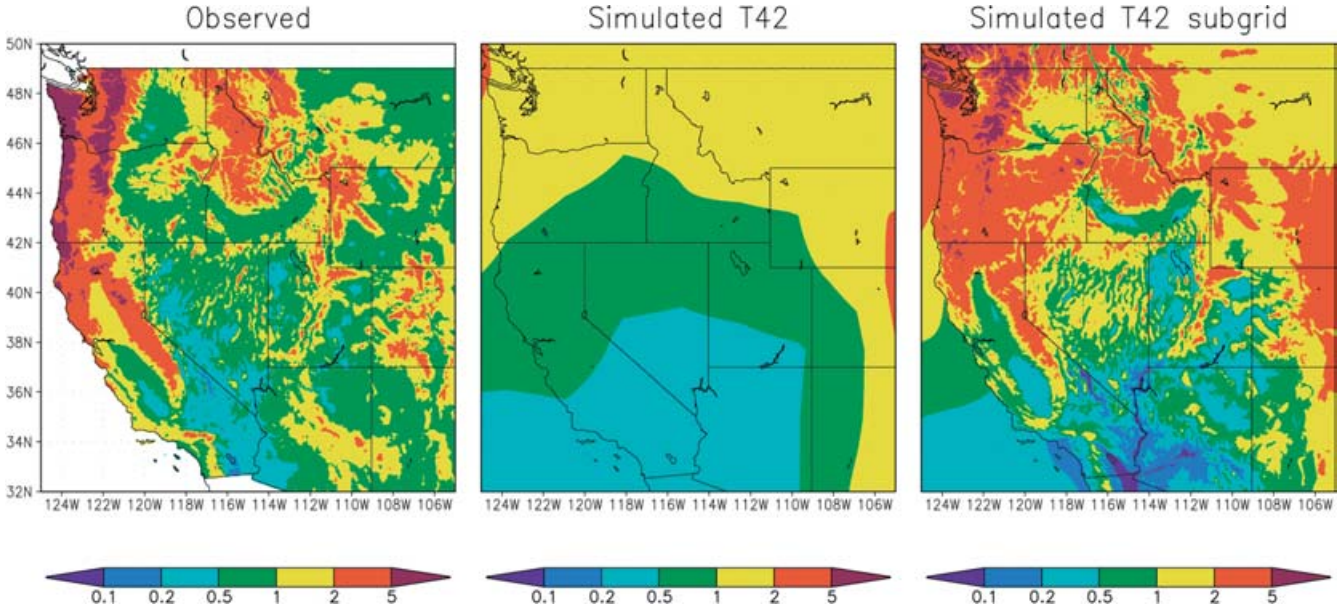

Fig. 7 Annual mean precipitation rate (mm/day) observed (*left*), simulated at T42 resolution without the subgrid scheme (*middle*) and simulated with the subgrid scheme (*right*), mapped to 2.5 minute resolution for the western USA

scheme captures much of the spatial structure of the precipitation rate, including minima in the basins and valleys and maxima in the mountain ranges in the western USA. However, it clearly misses the maxima along the coastline of Washington and Oregon and overestimates precipitation on the lee side of the Cascades and Sierra Nevada. To see the biases more clearly, Fig. 8 shows the ratio of the simulated/observed annual mean precipitation rate for the simulations with and without the subgrid scheme. The biases in the simulation with the subgrid scheme are much lower than in the simulation without. However, the simulation with the subgrid scheme underestimates precipitation on the windward side of the coastal ranges by 30–70% and overestimates precipitation on the lee side of the ranges by a factor exceeding two. These biases illustrate the

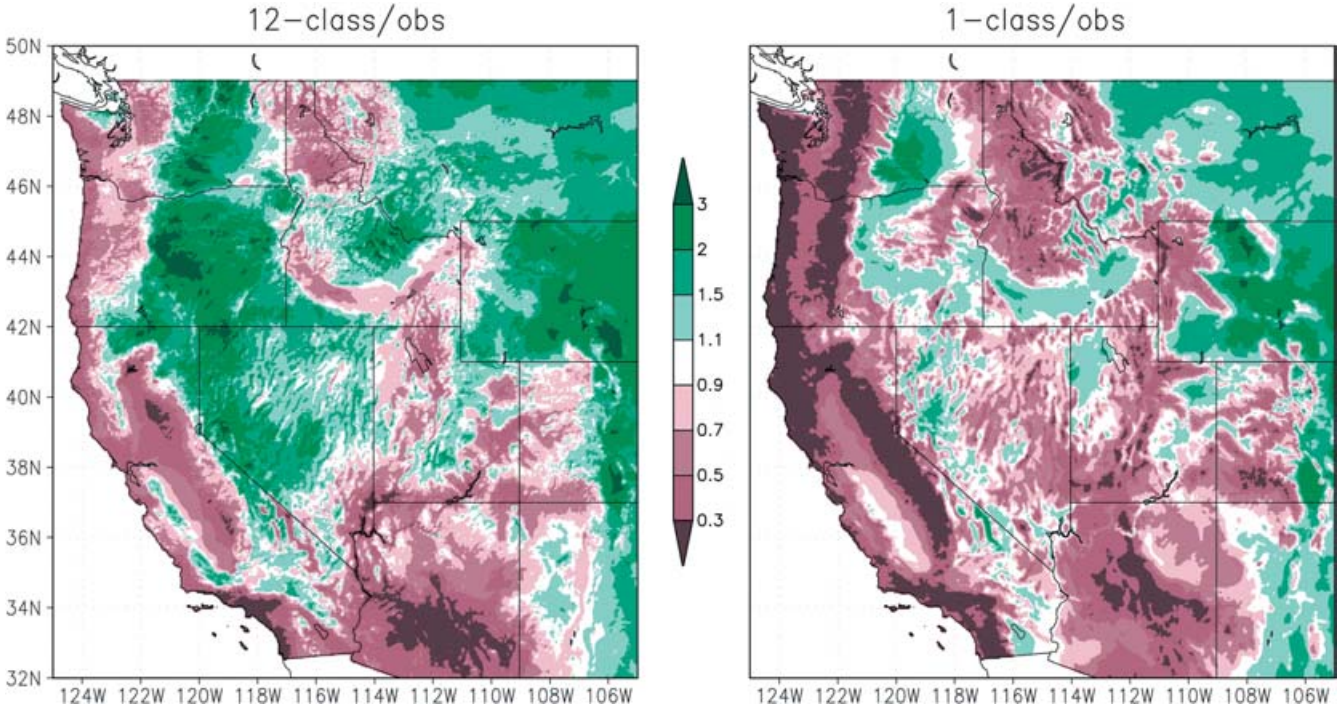

Fig. 8 Ratio of simulated/observed annual mean precipitation rate for the simulations with (*left*) and without (*right*) the subgrid scheme

absence of a treatment of rainshadow formation by the subgrid scheme. Rainshadow formation must be explicitly resolved, which clearly is not accomplished by the T42 resolution of these simulations; However, in almost all of the western USA the precipitation biases simulated with the subgrid scheme are smaller than those simulated without.

Another useful validation dataset is the snow water equivalent distribution estimated by the National Operational Hydrologic Remote Sensing Center (NOHRSC). It uses a statistical methodology (Hartman et al. 1995) to combine station measurements of snow water, satellite estimates of the snow line, and a digital surface elevation model to produce a gridded distribution of snow water at a resolution of 1.5 minutes (about 3 km) for the western USA. We have averaged the twice-weekly NOHRSC product over each month for the years 1995–2000. Figure 9 compares the March climatological "observed" snow water with that simulated with and without the subgrid scheme. The simulation without the subgrid scheme misses almost all of the spatial structure of the observed snow water distribution and would clearly be next to useless for climate impact studies. The simulation with the subgrid scheme captures much of the spatial structure, including maxima along the mountain ranges and minima in the basins and valleys. However, serious biases are evident. To see the biases more clearly, Fig. 10 shows the ratio of the simulated/observed March snow water for the simulations with and without the subgrid scheme. Biases are clearly much smaller with the subgrid scheme than without. In the simulation without the subgrid scheme snow water is less than 3% of observed for most of the mountains in the western USA, with somewhat better agreement with observations on the lee side of the Cascades and Sierra Nevada. In the simulation with the subgrid scheme snow water is underestimated by a factor of 2 to 5 in the Sierra Nevada, the Wasatch range in Utah, and in the Colorado Rocky Mountains, and overestimated by a factor of 2 to 5 in eastern Oregon and on the lee side of the Sierra Nevada.

To better understand the cause of the excessive snow bias in eastern Oregon, Fig. 11 shows the seasonal cycle of surface air temperature, precipitation, and snow water simulated with the subgrid scheme and observed at Aneroid Lake, a snow telemetry station at elevation 2225 m in the Wallowa Mountains of northeastern Oregon. The simulated values have been mapped to the elevation of the station. The model simulates far too much snow water, with a September minimum of 0.8 m that is greater than the observed April maximum. Part of the excessive snow is due to excessive precipitation (nearly twice as much precipitation in the simulation as observed), and part is due to the 3–5 °C cold bias (which both increases the snowfall during the transition seasons and reduces the snow melt). Thus, the excessive snow bias in eastern Oregon is due to both the cold bias evident throughout the western USA and the inability of the model to represent the rainshadow on the lee side of the Cascade and Sierra Nevada mountains.

Is the excessive snow accumulation on the lee side of mountain ranges in the western USA representative of the snow simulated elsewhere using the subgrid scheme? To answer this question we could use station measurements of snow depth and snow water equivalent for Canada (MSC 2000) and the former Soviet Union (NSIDC 1999), and global analyses of snow depth, snow cover and snow water equivalent at about 50 km resolution (Foster et al. 1996). Instead we explore the use of an alternate snow water validation dataset, namely the known worldwide distribution of glaciers. According to

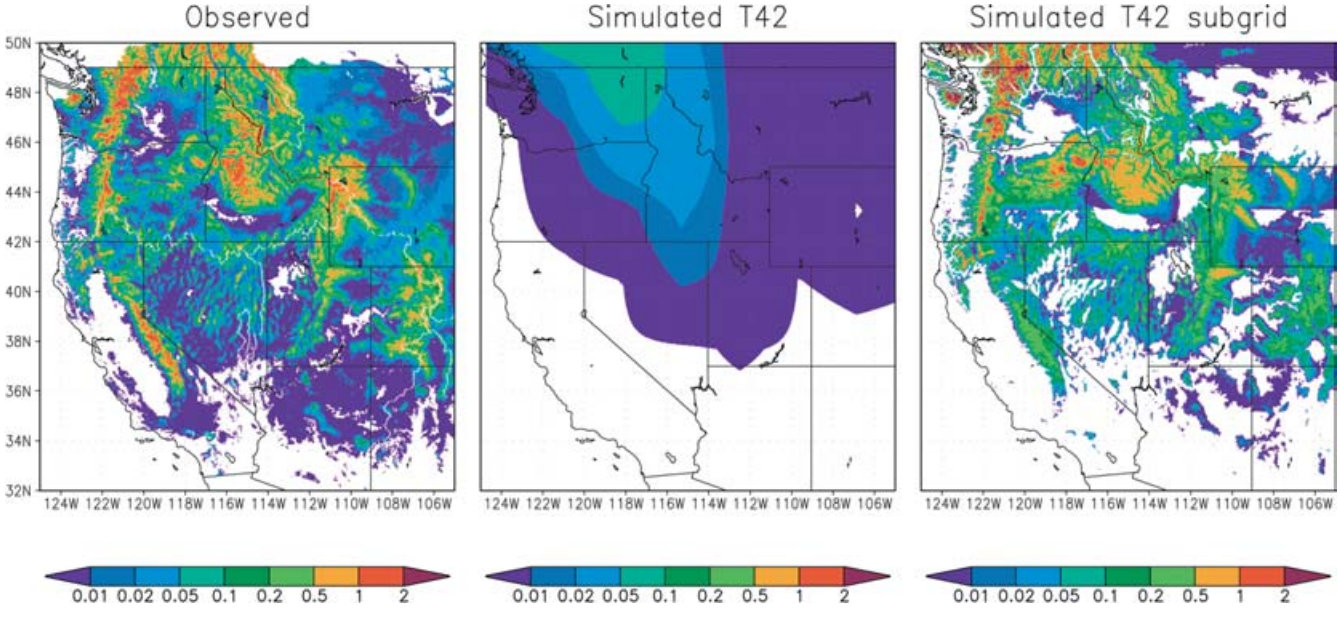

Fig. 9 Snow water equivalent (m) for March as observed (*left*) and as simulated at T42 resolution without the subgrid scheme (*middle*) and with the subgrid scheme (*right*), mapped to 1.5 minute resolution for the western USA

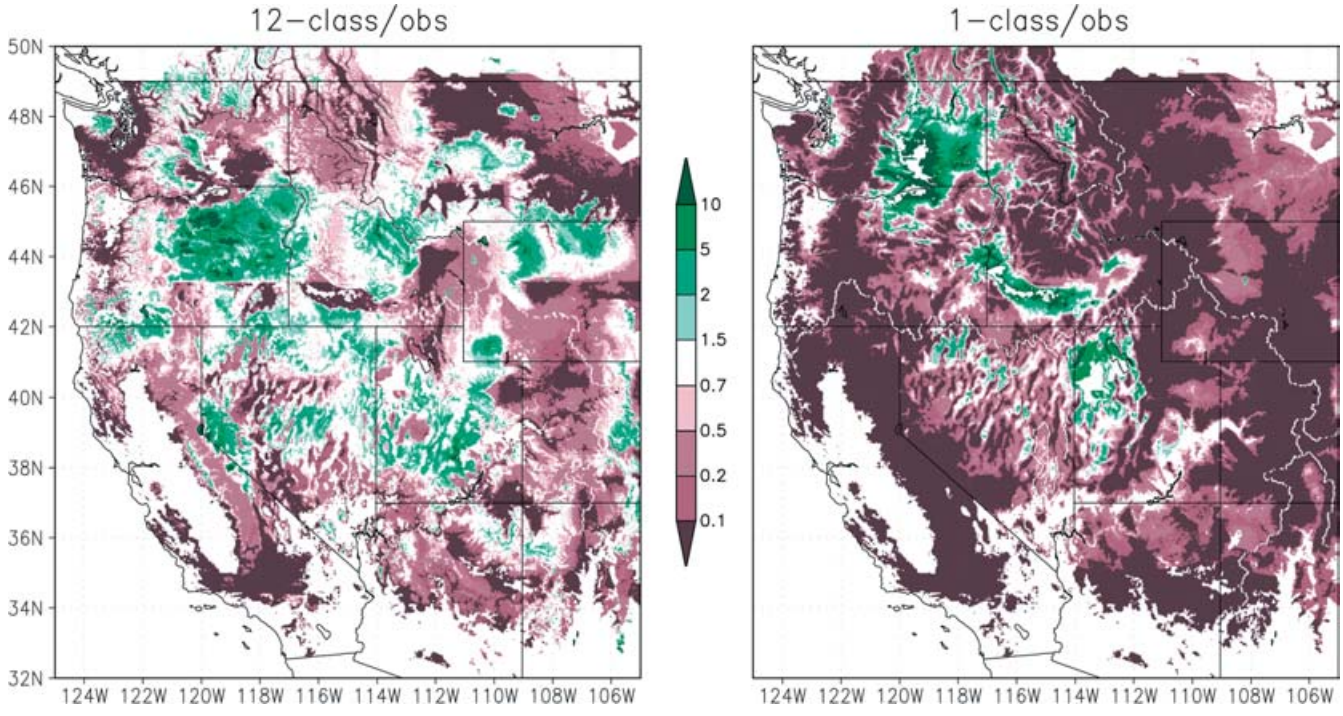

Fig. 10 Ratio of simulated/observed March snow water equivalent for the simulations with (*left*) and without (*right*) the subgrid scheme

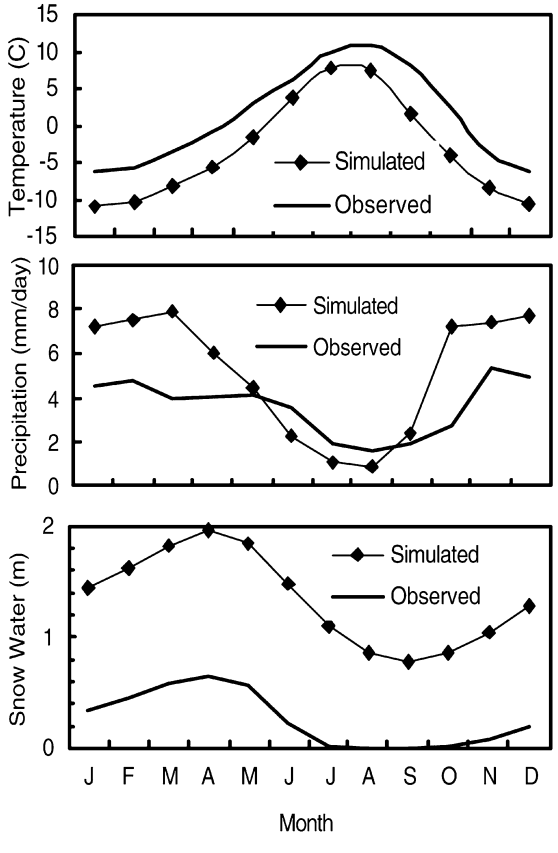

Fig. 11 Simulated and observed seasonal cycle of surface temperature, precipitation, and snow water equivalent at Aneroid Lake in the Wallowa Mountains of northeastern Oregon

the NOHRSC analysis and Fig. 11 the minimum snow water in the western USA typically occurs in August and September. Thus, it is reasonable to assume that the snow simulated for August is permanent in the Northern Hemisphere, and the snow simulated for February is permanent in the Southern Hemisphere. We can therefore compare the simulated summertime snow distribution with the observed glacier distribution. This is particularly illuminating as an integrated assessment because excessive permanent snow area indicates excessive precipitation and/or a cold bias, and too little permanent snow area indicates inadequate precipitation and/or a warm bias. Although lateral snow/ice transport plays a role in determining the observed distribution of glaciers and is not treated in the model, it is unlikely to play a major role on the 5 km scale represented here, except for the most dynamic glaciers. Although station measurements can provide more quantitative information about snow water, they are not available in many regions of the world. Global analyses do not provide the resolution needed in regions with complex terrain.

Figure 12 compares the observed distribution of glaciers in western North America with the snow water simulated for August using the subgrid scheme. The observed distribution is from the Global Land Ice Measurements from Space (http://www.GLIMS.org/icecheck.html) land ice dataset. The simulated snow water has been mapped to 2.5 minute (~5 km) resolution. The simulation correctly predicts permanent snow accumulation on the Canadian Rocky Mountains and on the coastal mountain ranges of Washington,

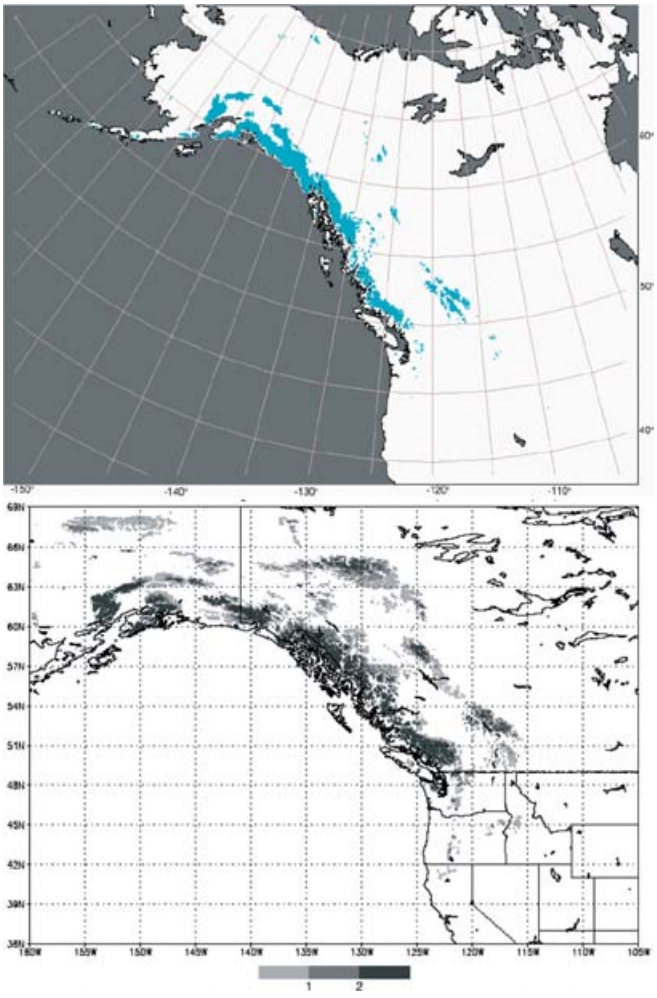

Fig. 12 Observed distribution of glaciers (*top*) and simulated distribution of August snow water equivalent (*bottom*) for northwestern North America

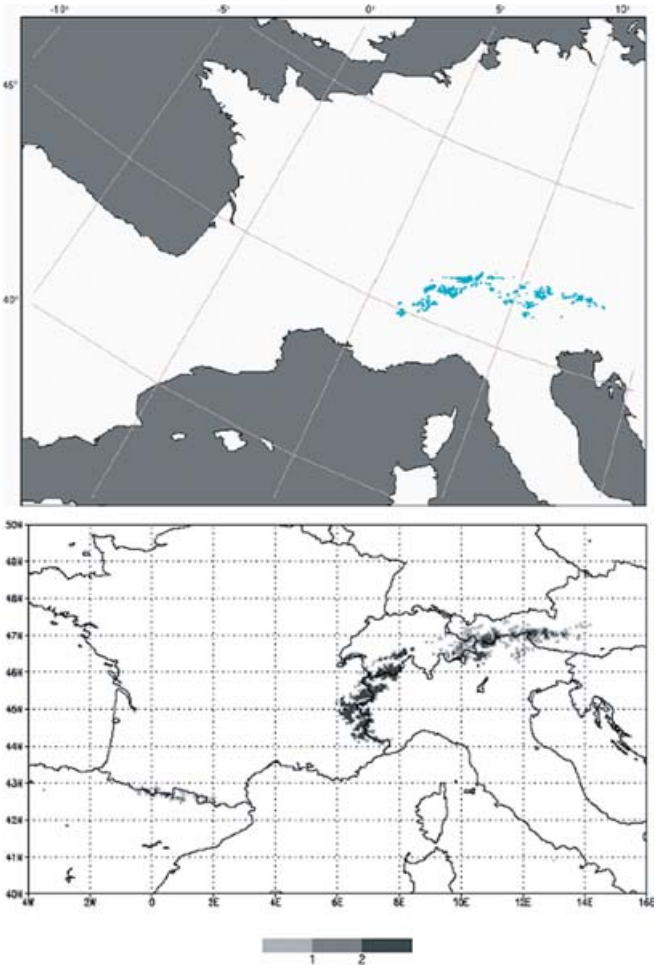

Fig. 13 Observed distribution of glaciers (*top*) and simulated distribution of August snow water equivalent (*bottom*) for central Europe

British Columbia, and Alaska, but incorrectly predicts permanent snow on most of the secondary inland ranges where glaciers are not observed. This bias again reflects the excessive precipitation simulated there. Too little moisture is being trapped by the coastal ranges, because they are represented as essentially a random distribution within each grid cell rather than as ridges acting like a roller for a floor mop.

Are these biases unique to North America? Figure 13 compares the observed distribution of glaciers in Europe with the snow water simulated for August using the subgrid scheme. The simulation exhibits the same tendency to overpredict permanent snow cover, with excessive snow area simulated in both the Alps and the Pyrenees. The same tendency to simulate excessive permanent snow area is also evident is other regions of the world, such as central Asia and South America (not shown). The bias is most evident on the lee side of the mountain ranges.

In an attempt to reduce the permanent snow bias we have repeated the simulation with the subgrid scheme, but with an orographic time scale of 20 h rather 10 h. This produces a weaker orographic signal in both temperature and precipitation. Although the summertime snow bias is reduced in the experiment, the orographic signature of precipitation is underestimated. This suggests that a simulation with a 20-h orographic time scale for temperature and a 10-h time scale for precipitation might produce a more realistic climate simulation. However, it is difficult to justify different orographic time scales for temperature and precipitation on physical grounds.

4 Computational burden

Although the subgrid scheme clearly improves the climate simulation in regions with complex terrain, the added realism does not come without a price: both the memory and run time required with the subgrid scheme are increased by a factor of at least two. Although such an increase pales in comparison with the cost of refining the grid resolution sufficiently to explicitly resolve the orographic signature in regions with complex terrain, it

is a higher price than some would want to pay, and hence requires some consideration.

The added computational burden arises from the application of all of the column physics (atmosphere and land surface) to each elevation class treated in each grid cell. If the computational burden of the column physics dominates that of the dynamical processes, then the computational burden is proportional to the number of elevation classes in each grid cell. Thus, an upper bound on the computational burden of the subgrid scheme can be determined from the number of elevation classes treated in each grid cell. For the set of 12 elevation classes considered in this study, the number of classes needed to account for the range of elevation in each T42 grid cell is illustrated in Fig. 14. The number of classes is heterogeneous, reflecting the global diversity of topography. Most grid cells are ocean and hence require only a single elevation class. Others contain a wide range of surface elevation and hence require as many as 11 elevation classes. Regions with complex topography generally require more elevation classes than regions with homogeneous topography.

If the climate model is run on a single processor computer then the upper bound on the computational impact of the subgrid scheme is simply the average number of elevation classes over all grid cells. For 12 elevation classes and T42 resolution, the average is 2.31. The memory required by the model with the subgrid scheme would accordingly increase by the same factor, but only if memory is added only for those classes needed by each grid cell. If the subgrid scheme is applied by simply adding an inner loop over elevation classes, with all variables dimensioned by the maximum number of classes (11), then the memory required would increase 11-fold. Clearly such a data structure is inefficient. A data structure that uses a single index to represent latitude, longitude and elevation class would most easily produce the lowest impact of the subgrid scheme on the memory requirements of the model. As an alternate, the longitude index could be used to represent elevation class as well as longitude, so that the memory required would be proportional to the maximum number of elevation classes in a latitude band.

If the climate model is run on multiple processors then load imbalances can increase the computational burden of the subgrid scheme. As an extreme example, if a single processor is devoted to each grid cell then the load imbalance is quite clearly illustrated in Fig. 14. Most grid cells would have only one elevation class and hence the processors assigned to those grid cells would sit idle most of the time while a few processors operate on as many as 11 elevation classes. Clearly load balancing is needed to reduce the computational burden of the subgrid scheme. Again, this can be achieved by using a single index to represent latitude, longitude, and elevation class, and distributing the computational burden of the column physics evenly across all processors.

For a one-dimensional domain-decomposition, which is commonly employed in climate models, the computational burden depends on the number of elevation classes in each latitude band. Figure 15 shows the average number of elevation classes as a function of latitude for the 12 elevation classes and spectral resolutions of T42 (2.8°), T84 (1.4°), and T168 (0.7°). The distribution of the load is still heterogeneous, though not as much as in the two-dimensional case. Some latitudes have an average of one class per grid cell, while others have as many as 3.9 at T42 resolution. At finer resolution, the number of elevation classes decreases because more variability of the topography is explicitly resolved. This resolution dependence is summarized in Table 2, which lists the global mean number of elevation classes per grid cell, the maximum number of elevation classes in a grid cell, and the maximum zonal mean number of elevation classes in a latitude band, for the 12 classes and spectral resolutions of T42, T84, and T168. The global mean number of elevation classes decreases from 2.31 at T42 resolution to 1.58 at T168 resolution. The global mean

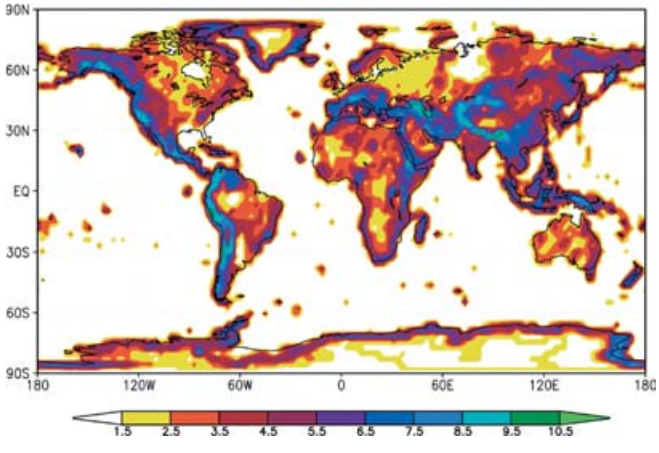

Fig. 14 Number of elevation classes per grid cell estimated for the T42 gaussian grid and the 12 class classification, using global 30 second digital elevation data

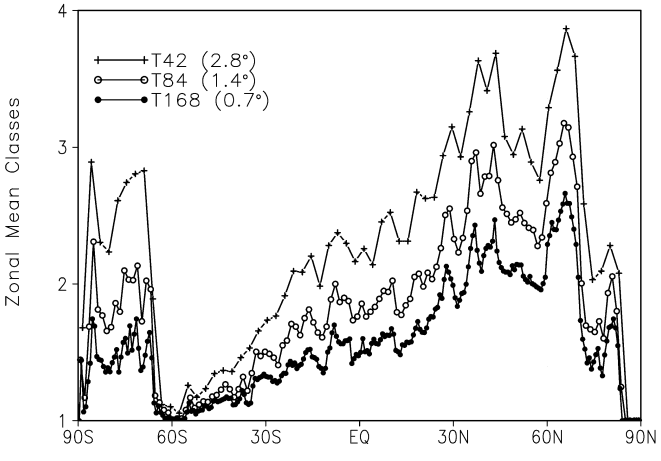

Fig. 15 Zonal mean number of elevation classes per grid cell for the T42, T84, and T168 gaussian grids, using the 12 class classification

Table 2 Global statistics of elevation classification

	Spectral resolution		
	T42 2.8°	T84 1.4°	T168 0.7°
Average classes per cell	2.31	1.86	1.58
Maximum classes in a cell	11	11	11
Maximum zonal mean classes per cell	3.9	3.2	2.7

will continue to decrease with finer resolution down to the 1 km resolution of the digital elevation dataset, which will yield only one class for all grid cells. Thus, the subgrid scheme has the desirable property of vanishing at increasingly fine resolution. There is no danger of double counting. The maximum number of elevation classes is less sensitive to resolution, remaining at 11 for all three resolutions. It will eventually decrease to one at 1 km resolution, but it appears to require quite fine resolution before it begins to decrease. The maximum zonal mean number of elevation classes per grid cell, which reflects the computational burden of the subgrid scheme for models using one-dimensional domain decomposition and reflects the memory burden if the longitude index is expanded to account for elevation class, decreases from 3.9 at T42 resolution to 2.7 at T168 resolution.

Such computational and memory requirements of the subgrid scheme are much larger than many users would want to carry. However, it is important to put such requirements in perspective. The memory and computations of the subgrid scheme pale when compared to those required to explicitly resolve the spatial structure achieved with the subgrid scheme. A ten-fold increase in resolution (from roughly 250 km to 25 km, which is marginally adequate) would increase the memory required by a minimum of a factor of 100 and the computation required by a factor of about 1000. Given the rate at which processor speeds are increasing and the obstacles to efficient parallelization of climate model codes, it will be at least a decade before such explicit resolution will be available to all but the most privileged and determined of model users. In the meantime, the subgrid scheme offers an alternate for achieving the resolution needed for many impact studies.

5 Conclusions

To summarize, an orographic subgrid scheme has been applied to a global climate model and evaluated through comparison with a variety of measurements. Although the subgrid scheme produces spectacular improvements in the simulation of some important climate fields (particularly snow water), systematic biases have been identified. These biases can be reduced through finer horizontal resolution. The resolution required to reduce the biases has been crudely estimated at about 50 km (LG 1995), but explicit simulations are required to confirm the expected improvements. Regional climate simulations with the subgrid scheme could play a role in identifying the resolution required to resolve the rainshadow that drives the biases.

The subgrid scheme introduces a computational burden of a factor of two to four, depending on the elevation classification, the explicit horizontal resolution, and the parallelization of the climate model. Such a burden is too large for some purposes. However, we have shown that the subgrid scheme modifies the grid cell means of only a few climate fields. This suggests that any tuning of the climate model run without the subgrid scheme will also apply to simulations with the subgrid scheme. Thus, the subgrid scheme can be supported without any additional tuning.

The subgrid scheme offers several advantages but also has some weaknesses. Strengths are that it:

1. Provides superior performance for precipitation and snow at lower computational cost than a doubling or quadrupling of resolution
2. Provides high resolution detail without high memory costs
3. Adds computations only in complex terrain
4. Is physically based
5. Does not affect the large-scale climatology of most fields
6. Applies to synoptic as well as climatic time scales
7. Computational and climatic impact decreases with increasing resolution, vanishing at resolutions approaching 1 km
8. Workload distribution is static and hence can be evenly distributed across processors

Weaknesses are:

1. The airflow model is relatively crude
2. The orographic forcing time scale τ is arbitrary
3. The influence of slope and aspect on surface processes is neglected
4. Precipitation in one elevation class does not influence precipitation in other classes
5. Does not treat rainshadows, which require grid size < 100 km
6. Introduces large load imbalance

Further work is needed to address several issues. First, the resolution dependence of the climate model performance with and without the subgrid scheme needs to be determined. Rainshadow formation will be better resolved at finer horizontal resolution both with and without the subgrid scheme, but we expect that at all resolutions simulations with the subgrid scheme will continue to be superior to simulations without the scheme.

Second, the dependence of the performance on the elevation classification needs to be more fully explored. We have briefly considered a five-class scheme and found

it to be clearly inferior to the 12-class scheme used in the simulation presented here. Finer elevation classification may improve the simulations without introducing a much larger computational and memory burden.

Third, the dependence of the performance on the orographic time scale needs to be more fully explored. We have considered a time scale of 20 h and found some improvements but also some new problems. Further investigation is warranted.

Fourth, the subgrid scheme needs to be tested in a frozen version of a climate model. The biases in the grid cell mean climate of ccm3.10 may be larger than those in the next generation of the ccm (cam2.0). Consideration of these issues is awaiting the release of the next generation climate model.

Beyond the exploration of these issues, the subgrid scheme could be further extended by introducing a subgrid elevation dependence of vegetation type. LG 1998 have shown that by using a separate vegetation type for each elevation class, the spatial variability of vegetation type can be better represented without any increase in the computational or memory burden.

Although the developmental version of the climate model (ccm3.10) is not available for public release, this study signals the release of the preprocessing and postprocessing codes required to (a) determine the number of elevation classes, the fractional area and the average elevation of each elevation class in each grid cell, (b) form grid cell means of the predictions for each elevation class, and (c) distribute the predictions for each elevation class according to the high-resolution distribution of surface elevation. The postprocessing codes have been written specifically for processing atmosphere and land surface netcdf history files produced by the NCAR ccm at any resolution. The coding of the subgrid scheme will be released after it has been applied to the next generation of the ccm (cam2.0).

This work also signals the release of a 1.5 minute resolution gridded snow water equivalent climatology for the western USA for the each month during water years 1995–2000.

Acknowledgements The work reported here was funded by the US Department of Energy Environmental Science Division Climate Change Prediction Program. The Pacific Northwest National Laboratory is operated for the DOE by Battelle Memorial Institute under contract DE-AC06-76RLO 1830. The PNNL Molecular Science Computing Facility provided the computer time on the IBM SP2 used for the climate model simulations. The authors kindly acknowledge the limited distribution of the ccm3.10, developed by the NCAR Community Climate System Model Atmospheric Model Working Group. Rick Wessels, Bruce Raup and Trent Hare of USGS prepared the glacier distribution figures as part of the NASA GLIMS project.

References

Bonan GB (1998) The land surface climatology of the NCAR Land Surface Model coupled to the NCAR Community Climate Model. J Clim 11: 1307–1326

Collins WD (2001) Parametrization of generalized cloud overlap for radiative calculations in general circulation models. J Atmos Sci 58: 3224–3242

Cubasch U, Waszkewitz J, Hegerl G, Perlwitz J (1995) Regional climate changes as simulated in time-slice experiments. Clim Change 31: 273–304

Daly C, Neilson RP, Phillips DL (1994) A statistical-topographic model for mapping climatological precipitation over mountainous terrain. J Appl Meteorol 33: 140–158

Daly C, Taylor G, Gibson W (1997) The PRISM approach to mapping precipitation and temperature, 10th Conf on Applied Climatology, Reno, Nevada, American Meteorological Society, pp 10–12

Delworth TL, Knutson TR (2000) Simulation of early 20th century global warming. Science 287 (5461): 2246–2250

Dickinson RE, Errico RM, Giorgi F, Bates GT (1989) A regional climate model for western United States. Clim Change 15: 383–422

Emori S, Nozawa T, Abe-Ouchi A, Numaguti A, Kimoto M, Nakajima T (1999) Coupled ocean–atmosphere model experiments of future climate change with an explicit representation of sulfate aerosol scattering. J Meteorol Soc Japan 77: 1299–1307

Flato GM, Boer GJ, Lee WG, McFarlane NA, Ramsden D, Reader MC, Weave AJ (2000) The Canadian Centre for Climate Modelling and Analysis global coupled model and its climate. Clim Dyn 16: 451–467

Foster J, Liston G, Koster R, Essery R, Behr H, Dumenil L, Veseghy D, Thompson S, Pollard D, Cohen J (1996) Snow cover and snow mass intercomparisons of general circulation models and remotely sensed datasets. J Clim 9: 409–426

Ghan SJ (1992) The GCM credibility gap. Editorial, Clim Change 21: 345–346

Giorgi F (1990) Simulation of regional climate using a limited area model nested in a general circulation model. J Clim 3: 941–963

Giorgi F, Mearns LO (1999) Introduction to special section: regional climate modeling revisited. J Geophys Res 104: 6335–6352

GLOBE Task Team and others (Hastings DA, Dunbar PK, Elphingstone GM, Bootz M, Murakami H, Maruyama H, Masaharu H, Holland P, Payne J, Bryant NA, Logan TL, Muller J-P, Schreier G, MacDonald JS) eds. (1999) The Global Land One-kilometer Base Elevation (GLOBE) Digital Elevation Model, Version 1.0. National Oceanic and Atmospheric Administration, National Geophysical Data Center, 325 Broadway, Boulder, Colorado 80303, USA. Digital data base on the World Wide Web (URL: http://www.ngdc.noaa.gov/seg/topo/globe.shtml) and CD-ROMs

Gordon C, Cooper C, Senior CA, Banks HT, Gregory JM, Johns TC, Mitchell JFB, Wood RA (2000) The simulation of SST, sea ice extents and ocean heat transports in a version of the Hadley Centre coupled model without flux adjustments. Clim Dyn 16: 147–168

Gyalistras D, Schär C, Davies HC, Wanner H (1998) Future Alpine climate. In: Cebon P, Dahinden U, Davies HC, Imboden D, Jaeger CC (eds) Views from the Alps. Regional perspectives on climate change. Massachusetts: MIT Press, Cambridge, pp 171–223

Hartman RK, Rost AA, Anderson DM (1995) Operational processing of multi-source snow data. Proc Western Snow Conference, pp 147–151

Kiehl JT, Hack JJ, Bonan GB, Boville BB, Williamson DL, Rasch PJ (1998) The National Center for Atmospheric Research Community Climate Model: CCM3. J Clim 11: 1131–1149

Leung LR, Ghan SJ (1995) A subgrid parametrization of orographic precipitation. Theor Appl Climatol 52: 95–118

Leung LR, Ghan SJ (1998) Parametrizing subgrid orographic precipitation and surface cover in climate models. Mon Weather Rev 126: 3271–3291

Leung LR, Wigmosta MS, Ghan SJ, Epstein DJ, Vail LW (1996) Application of a subgrid orographic precipitation/surface

hydrology scheme to a mountain watershed. J Geophys Res 101: 12,803–12,817

May W, Roeckner E (2001) A time-slice experiment with the ECHAM4 AGCM at high resolution: the impact of resolution on the assessment of annual mean climate change. Clim Dyn 17: 407–420

MSC (2000) Canadian Snow Data CD-ROM. CRYSYS Project, Climate Processes and Earth Observation Division, Meteorological Service of Canada, Downsview, Ontario, Canada

Murphy JM (1999) An evaluation of statistical and dynamical techniques for downscaling local climate. J Clim 12: 2256–2284

Murphy JM (2000) Predictions of climate change over Europe using statistical and dynamical downscaling techniques. Int J Climatol 20: 489–501

NSIDC (1999) Historical soviet daily snow depth. CD-ROM, National Snow and Ice Data Center, Cooperative. Institute for Research In Environmental Science, University of Colorado, Boulder, CO 80,309-0449 USA

Rasch PJ, Kristjánsson JE (1998) A comparison of the CCM3 model climate using diagnosed and predicted condensate parametrizations. J Clim 11: 1587–1614

Russell GL, Rind D (1999) Response to CO_2 transient increase in the GISS coupled model: regional coolings in a warming climate. J Clim 12: 531–539

von Storch H (1995) Inconsistencies at the interface of climate impact studies and global climate research. Meteorol Z 4 NF, 72–80

Washington WM, Weatherly JM, Meehl GA, Semtner AJ Jr, Bettge TW, Craig AP, Strand WG, Arblaster J, Wayland VB, James R, Zhang Y (2000) Parallel climate model (PCM) control and transient simulations. Clim Dyn 16: 755–774

Wilby RL, Wigley TML (1997) Downscaling general circulation model output: a review of methods and limitations. Prog Phys Geogr 21: 530–548

Williamson DL, Olson JG (1994) Climate simulations with a semi-Lagrangian version of the NCAR community climate model. Mon Weather Rev 122: 1594–1610

Xie P, Arkin PA (1996) Analyses of global monthly precipitation, using gauge observations, satellite estimates, and numerical model predictions. J Clim 9: 840–858

Zhang X-H, Shi G-Y, Liu H, Yu Y-Q (eds) (2000) IAP global atmosphere–land system model. Science Press, Beijing, China, pp 259